Electric-field control of interfacial in-plane magnetic anisotropy in CoFeB/MgO junctions

doi: https://doi.org/10.1103/PhysRevB.101.174405

Electric-field control of interfacial in-plane magnetic anisotropy in CoFeB/MgO junctions

Angshuman Deka[1], Bivas Rana[2], Ryo Anami[1], Katsuya Miura[3], Hiromasa Takahashi[3], YoshiChika Otani[2, 4], and Yasuhiro Fukuma[1, 2*]

[1] *Department of Computer Science and Electronics, Kyushu Institute of Technology, 680-4 Kawazu, Iizuka 820-8502, Japan*

[2] *Center for Emergent Matter Science, RIKEN, 2-1 Hirosawa, Wako 351-0198, Japan*

[3] *Research and Development Group, Hitachi Ltd., 1-280 Higashi-koigakubo, Kokubunji 185-8601, Japan*

[4] *Institute for Solid State Physics, University of Tokyo, Kashiwa, Chiba 277-8581, Japan*

Correspondence should be addressed to Y.F. (fukuma@cse.kyutech.ac.jp)

Abstract

Magneto-electric coupling in metal/oxide heterostructures has opened up the possibility of controlling magnetization by voltage i.e. electric-field. However, the electric-field excitation of magnetization dynamics in perfectly in-plane and out-of-plane magnetized films have not been demonstrated so far due to zero electric-field torque originated from voltage control of perpendicular magnetic anisotropy. This limits the application of voltage controlled magnetic anisotropy in magnetic field free control of magnetization dynamics. Here, we show that magnetic annealing can induce an interfacial in-plane magnetic anisotropy of CoFeB/MgO junctions thereby controlling the symmetry of interfacial magnetic anisotropy. The magnetic anisotropy is modulated by applying voltage: a negative bias voltage increases perpendicular magnetic anisotropy, while a positive bias voltage decreases perpendicular magnetic anisotropy and increases the in-plane magnetic anisotropy. Such a control of symmetry of the interfacial magnetic anisotropy by magnetic annealing and its tunability by electric-fields is useful for developing purely voltage-controlled spintronic devices.

I. INTRODUCTION

Recent discoveries such as spin-transfer torque, spin-orbit torque and electric-field torque provide a new strategy for designing future spintronic devices which require power efficient excitation of magnetization dynamics. In this regard, spin-transfer torque has been mainly utilized for exciting the magnetization dynamics in magnetic nano-structures [1,2]. However, there is an inevitable effect of Joule heating because of a high charge current density of ~10^{11} A/m^2 in the devices. Spin-orbit torques generated at an interface between non-magnetic metals with strong spin-orbit interaction and ferromagnetic metals could be a promising approach for energy-efficient manipulation [3,4], yet recently reported charge current densities required for magnetization switching or exciting spin waves remain too large to be ignored [5,6]. Further significant reduction of power consumption is envisaged by voltage-controlled magnetic anisotropy (VCMA) wherein electric-fields can be used to control magnetization [7].

The effect of an electric-field on magnetic properties has been reported for various systems, such as magnetic semiconductors, multiferroic materials and magnetic metal/oxide bilayers [8]. In particular, CoFeB/MgO junctions have attracted much attention because of its great potential to realize ultra-low power spintronic nanodevices, thanks to its giant tunneling magnetoresistance [9,10] and strong perpendicular magnetic anisotropy (PMA) [11]. The magneto-electric coupling at the CoFeB/MgO interface allows us to control magnetization

dynamics, such as ferromagnetic resonance (FMR) excitation, magnetization switching and spin wave excitation, by using electric-fields [7,12-17]. One mechanism to explain the electric-field effect is that magnetic anisotropy energy is changed by selective electron-hole doping into 3*d* orbitals of the interfacial ferromagnetic atoms through spin-orbit interaction [18,19]. This interfacial PMA shows uniaxial symmetry where its energy is expressed in the form of $K_{u\perp}\sin^2\theta$, with $K_{u\perp}$ being the uniaxial PMA energy and θ being the elevation angle of the magnetization from the film plane. The corresponding electric-field torque caused by VCMA is estimated to be a function of $\sin\theta\cos\theta$ obtained from the derivative of the energy terms. Therefore, VCMA experiments have so far used an external magnetic field for titling the magnetization direction because electric-field torque is zero in the in-plane (θ = 0 degree) or out-of-plane (θ = 90 degree) magnetized samples [7]. However, a non-zero electric-field torque is expected for the in-plane magnetized films if the interfacial magnetic anisotropy has an in-plane uniaxial component $K_{u,//}$, which is expressed in the form $K_{u//}\cos^2\theta\cos^2\phi$, ϕ being the azimuthal angle. Such a modification of the electric-field torque offers an interesting opportunity to explore purely voltage-controlled spintronic devices. VCMA of an in-plane magnetic anisotropy is reported for semiconducting (Ga,Mn)As thin films [20] and Fe/n-GaAs Schottky junctions [21]. There is so far no report about the interfacial in-plane magnetic anisotropy for the CoFeB/MgO junctions.

In this paper, we demonstrate that the magnetic annealing can be utilized not only to

enhance the typical PMA of CoFeB/MgO junctions, but also to induce an in-plane magnetic anisotropy (IMA). First, we describe the process of estimating the magnetic anisotropy fields. Then, using the obtained expression we quantify the effect of magnetic annealing on the magnetic anisotropy fields. Subsequently, we demonstrate that temperature dependence of both PMA and IMA can follow power law of its saturation magnetization with an exponent of ~2, implying an interfacial origin. Finally, we present our results on the electric-field effect on magnetic anisotropy fields using electrical detection of FMR. The VCMA behavior is clearly observed for both PMA and IMA at room temperature.

II. ESTIMATION OF MAGNETIC ANISOTROPY FIELDS

The derivation of a relationship between a resonant magnetic field of FMR and an azimuthal angle of the magnetization for an in-plane magnetized film, used for the estimation of magnetic anisotropy field of PMA and IMA, is described in this section. Let us consider that the direction of the magnetization M and external magnetic field H_{ex} is given by (ϕ, θ) and (α, β), respectively, where α and ϕ are the azimuthal angles and β and θ are the elevation angles from the film plane. The magnetic free energy F can be expressed as a sum of the Zeeman energy, demagnetization energy and magnetic anisotropy energy as below:

$$F = \frac{\mu_0 M_s}{2}\begin{bmatrix} -2H_{ex}(\cos\theta\cos\beta\cos(\alpha-\phi)+\sin\theta\sin\beta)+(M_s-H_p)\sin^2\theta \\ -H_k\cos^2\phi\cos^2\theta \end{bmatrix}, \qquad (1)$$

where H_k is the in-plane anisotropy field directed along $\phi = \theta = 0^o$, H_p is the perpendicular magnetic anisotropy field along $\theta = 90^o$.

Next we substitute F in the Smit-Beljers' relation [22] given by:

$$\left(\frac{f}{\gamma}\right)^2 = \left[M_s \cos\theta\right]^{-2}\left(\frac{\partial^2 F}{\partial\theta^2}\frac{\partial^2 F}{\partial\phi^2} - \left(\frac{\partial^2 F}{\partial\theta\partial\phi}\right)^2\right), \quad (2)$$

where f is the frequency and γ is the gyromagnetic ratio. We can obtain the free energy differentials with respect to ϕ and θ as below:

$$\frac{\partial^2 F}{\partial\theta^2} = \mu_0 M_s\begin{bmatrix} -H_{ex}\left(-\sin\theta\sin\beta - \cos\beta\cos(\alpha-\phi)\cos\theta\right) - (M_s - H_p)\cos 2\theta \\ -H_k\cos^2\phi\sin 2\theta \end{bmatrix}, \quad (3)$$

$$\frac{\partial^2 F}{\partial\phi^2} = \mu_0 M_s\left[H_{ex}\left(\cos\theta\cos\beta\cos(\alpha-\phi)\right) + H_k\cos^2\theta\cos 2\phi\right], \quad (4)$$

$$\frac{\partial^2 F}{\partial\theta\,\partial\phi} = -\mu_0 M_s\left[H_{ex}\left(\sin\theta\cos\beta\sin(\alpha-\phi)\right) + \frac{H_k}{2}\sin 2\theta\sin 2\phi\right]. \quad (5)$$

In this study, FMR measurements were performed for in-plane magnetized films in the condition that M is parallel to H_{ex}, in order to determine H_p and H_k. Using $\theta = \beta = 0^o$ and $\phi = \alpha$ in Eq. (3) ~ Eq. (5) and substituting the resulting expressions in Eq. (2), we obtain:

$$\left(\frac{f}{\gamma}\right)^2 = \frac{1}{M_s^2}\left(\left(\mu_0 M_s H_{ex} + \mu_0 M_s(M_s - H_p) + \mu_0 M_s H_k\cos^2\phi\right)\left(\mu_0 M_s H_{ex} + \mu_0 M_s H_k\cos 2\phi\right)\right). \quad (6)$$

Replacing H_{ex} with the term of resonant magnetic field H_{res} in Eq. (6), we obtain the relation between H_{res} and ϕ as below:

$$H_{res} = -H_k + \frac{3}{2}H_k \sin^2\phi - \frac{(M_s - H_p)}{2} + \frac{1}{2}\left[\begin{array}{l} H_k^2 \sin^4\phi + (M_s - H_p)^2 + 2(M_s - H_p)H_k \sin^2\phi \\ + 4\left(\frac{f}{\mu_0\gamma}\right)^2 \end{array}\right]^{\frac{1}{2}}. \quad (7)$$

III. EXPERIMENTAL DETAILS

Multilayer stacks of Ta(5)/Ru(10)/Ta(5)/$Co_{20}Fe_{60}B_{20}$(t)/MgO(2)/Al_2O_3(10) were sputtered at room temperature onto thermally oxidized Si(100) substrates at a base pressure of ~1×10^{-7} Pa. The nominal thicknesses of each layer mentioned in the parentheses are in nanometers (nm). The Al_2O_3 layer serves as a capping layer to maintain the quality of the MgO layer which is very important for interfacial magnetic anisotropy. Samples were annealed in a vacuum level of ~ 1×10^{-3} Pa, at different temperatures ranging from 100 °C to 400 °C in the presence of a magnetic field $\mu_0 H_b$ = 500 mT. The magnetization versus external magnetic field (*M-H*) curves and were measured by superconducting quantum interference device (SQUID) magnetometer. The saturation magnetization M_s was measured for the samples annealed at different temperatures upto 600 °C. M_s was found to be constant at 1.5 T upto 400 °C beyond which it drastically reduced to 450 mT. Such a drastic decrease in the M_s is expected to arise from the interdiffusion of the ultrathin ferromagnetic layer with the heavy metal underlayer at high annealing temperatures [23].

Broadband FMR measurements were used to estimate the magnetic anisotropy of samples. The sample was cut into pieces of a size < 2×2 mm^2 and then were placed face down

on coplanar waveguide (CPW) as shown in Fig. 1(a). The end of the CPW was connected to a port of a vector network analyzer and then a microwave field h_{rf} was applied to the samples by electromagnetic induction coupling. The reflection parameter (S_{11}) was measured at fixed microwave frequency by varying an in-plane external magnetic field.

For the electrical detection of FMR using spin pumping and inverse spin Hall effect (ISHE) measurements, the multilayer structure was firstly patterned into a rectangular shape of 10×200 μm^2 by using photolithography and Ar-ion milling. The bottom electrodes for detecting ISHE voltage from the Ta layer underneath of the CoFeB layer and the top electrode on the Al_2O_3 layer for applying voltage were fabricated by lift-off processes. Finally, a 200-nm-thick Ti/Au CPW for the application of microwave magnetic field was deposited adjacent to the multilayer structure with the rectangular shape. The amplitude of the microwave signal was modulated with a frequency of 79 Hz and then ISHE voltage was detected by a standard lock-in technique across the bottom electrodes in the Ta layer.

IV. RESULTS AND DISCUSSION

A. Effect of magnetic annealing on magnetic anisotropy

An example of the real and imaginary parts of the S_{11} parameter recorded in the FMR measurement is shown below the setup in Fig. 1(a). The obtained data are fitted by:

$$\Delta S_{11} = \frac{L \times dH^2}{(H_{ex} - H_{res})^2 + dH^2} + \frac{D \times dH \times (H_{ex} - H_{res})}{(H_{ex} - H_{res})^2 + dH^2} + a \times H_{ex} + b, \quad (8)$$

where L and D are the weights of the Lorentzian and dispersive parts, respectively, dH is the half width at half maximum, a and b are constants. In case of a sample with 2.0-nm thick CoFeB layer annealed at 200 ºC in the presence of $\mu_0 H_b$ = 500 mT perpendicular to the film plane, $\mu_0 H_{res}$ = 80.3 mT is obtained at the microwave frequency f = 6.0 GHz.

Subsequently, we study the effect of H_b on magnetic anisotropy of the samples. For comparison, we first measure the in-plane angular dependence of H_{res} of the films prior to annealing from which we can obtain $\mu_0 H_k$ and $\mu_0 H_p$ as 1.0 and 966 mT. Such an in-plane anisotropy typically appears in random directions during the deposition process. When the films are annealed in the presence of a bias field H_b in an in-plane direction which is perpendicular to the *inherent* in-plane magnetic anisotropy (x-axis), we observe minima along ϕ = 0 degree in the H_{res} vs ϕ plots as shown (red) in Fig. 1(b). On the other hand, if we anneal the films with H_b parallel to the *inherent* anisotropy of the films (y-axis), we can see a 90 degree phase difference between x- and y-axial annealing. Meanwhile, if we anneal the films with H_b perpendicular to the sample plane (z-axis), the amplitude of the sinusoidal behavior for H_{res} vs ϕ is clearly suppressed (blue). Upon fitting the experimental data in Fig. 1(b) using Eq. (7), we can obtain $\mu_0 H_k$ and $\mu_0 H_p$ as 1.3 and 1083 mT, 1.8 and 1088 mT, 0.4 and 1096 mT for the *x*-, *y*-, *z*-axis magnetic annealing, respectively. The small in-plane component for perpendicular H_b and the different magnitude of the anisotropy field between *x*- and *y*- axis magnetic fields may be due to the misalignment in the experimental setup during the

annealing.

In order to see the effect of annealing temperature on magnetic anisotropies, we measure the H_k and H_p as shown in Figs. 1(c) and 1(d), respectively, for different CoFeB thicknesses of 1.5 nm, 1.8 nm and 2.0 nm. Please note that H_k in all the samples were induced by annealing. It is observed that H_k for all the thicknesses decrease with increasing annealing temperature. On the other hand, H_p increases with increasing annealing temperature, reaching to a maximum at around 300 °C, and then drastically decreases with the further increment of annealing temperature because of intermixing of the interface, as reported in previous studies [23,24]. There have been many experimental and theoretical studies on IMA induced by magnetic annealing for bulk samples. The easy axis of the IMA is parallel to the direction of an external magnetic field during annealing. One plausible model to explain its mechanism in a cubic lattice such as NiFe and CoFe is directional ordering of atomic pairs: in alloys consisting of A and B atoms, an anisotropic distribution of different atom pairs such as AA, BB and AB yields a uniaxial anisotropy [25-28]. In this study, H_k decreases with increasing annealing temperature because migration of atoms causes an isotropic distribution of atom pairs among Co, Fe and B. Higher temperature annealing leads to improved crystallinity as well as atomic order at CoFeB/MgO interface [29], and therefore H_p is enhanced as shown in Fig. 1(d).

B. Temperature dependence of magnetization and magnetic anisotropy

The temperature dependence of saturation magnetization M_S(T) was measured using SQUID. The corresponding data for the 2.0-nm-thick CoFeB layer annealed at 200 ºC is shown in Fig. 2(a). The monotonic change with respect to temperature implies that the annealing process does not give rise to any oxide interlayer in the CoFeB/MgO junctions [30]. A decrease in the saturation magnetization at higher temperatures is due to the increment of thermal fluctuations and excitation of spin wave modes that tends to destabilize the orientation of magnetic moments. The experimental data were fitted using the Bloch's law $M_s(T) = M_s(0)\left(1-\left(\frac{T}{T_C}\right)^{\chi}\right)$, where T_C is the Curie temperature and χ is the Bloch's exponent. Upto T = 50 K, the experimental data fits well to the Bloch's law using T_C = 1150 K and χ = 1.5 as shown by the green line in Fig. 2a. The data in the measurement range of 50 K to 300 K was fitted to the Bloch's law using T_C = 1150 K and χ = 1.8 as shown by the red line in the same figure. A difference in the exponents between lower and higher measurement temperatures can be expected due to the magnon-magnon scattering [31].

The temperature dependence of anisotropy fields, H_p and H_k, of the corresponding sample were estimated using temperature dependent FMR measurements. Both H_p and H_k are found to be increased monotonically with decreasing temperature as shown in Fig. 2(b). Figure 2(c) shows the temperature dependence of the corresponding magnetic anisotropy energies. Since

the dominant contribution to PMA in CoFeB/MgO junctions comes from the interface between the two layers, we can approximately equate K_i/t, K_i being the interfacial PMA, to the energy corresponding to the PMA field $K_{u\perp}(T) = \frac{M_s(T)H_p(T)}{2}$ [32]. The experimental data are then fitted to the Callen-Callen power law of the magnetization [33] which can be written as $\frac{K_{u\perp}(T)}{K_{u\perp}(0)} = \left(\frac{M_s(T)}{M_s(0)}\right)^{\gamma}$ using scaling exponent γ = 2.1. According to the Callen-Callen model, the anisotropy energy scales as a function of temperature with γ = 3 for a ferromagnet, which has a single site origin of magnetic anisotropy. However, a scaling exponent of $\gamma \sim 2$ has been observed in VCMA systems with interfacial magnetic anisotropies like Ta/CoFeB/MgO [32,34,35] and Ru/Co_2FeAl/MgO [36]. Such a deviation from the Callen-Callen model is due to the presence of interfacial hybridization between the 3*d* orbitals of Fe and 2*p* orbitals of O atoms in the CoFeB/MgO junction. Upon estimating the energy corresponding to IMA $K_{u//}$ using a similar relation, as shown in Fig. 2(c), we are able to fit the temperature dependence of the anisotropy energies to the power law of magnetization using γ = 2.3. This indicates that, in addition to PMA, even IMA can have interfacial origin of the CoFeB/MgO junction.

C. Electric-field control of interfacial magnetic anisotropy

We study the electric-field effect on H_k and H_p of the CoFeB/MgO junction via spin

pumping and ISHE measurements. The optical microscope image of the device used in this process is shown in Fig. 3(a). The FMR signal was detected electrically by using ISHE as shown in Fig. 3(b). In this setup, the microwave magnetic field h_{rf} was applied perpendicular to the CoFeB layer from a nearby CPW. When FMR occurs, spin pumping generates spin current at the interface between CoFeB and Ta and then the spin current is converted into charge current via ISHE in the Ta layer. Figure 3(c) shows the detected ISHE voltage V_{ISHE} as a function of an external magnetic field H_{ex} for f from 1.0 GHz to 4.0 GHz. The V_{ISHE} signal shows the sign reversal with respect to the direction of H_{ex}, implying inverse spin Hall effect origin of measured signals.

It is reported that the line shape of the rectification voltage in spin pumping measurements strongly depends upon the microwave magnetic field distribution in the sample and contributions from anomalous Hall effect (AHE) or anisotropic magnetoresistance (AMR) [37]. According to Harder *et al.*, in this setup, AHE and AMR of the ferromagnet shows dispersive and Lorentzian lineshape, respectively, and ISHE shows Lorentzian lineshape. However, the AMR and ISHE spectra amplitudes show angular dependent behavior of the types sin2ϕ and sinϕ respectively. An angular dependent measurement in our devices revealed purely Lorentzian line shape of V_{ISHE} spectra whose amplitude has a sinϕ dependence. This confirms that the rectified voltage originates from inverse spin Hall effect where the FMR is excited by a z-axial microwave field. The magnitude of the rectification

voltage in the spectra increases with increasing frequency up to 3.0 GHz, and then starts to decrease with the further increase of frequency. This behavior is due to the fact that the spin current increases with increasing frequency for the spin pumping mechanism, but the increase of H_{ex} during FMR decreases the cone angle of magnetization precession, and therefore the generation of the spin current is suppressed at high frequencies [38]. The dependence of V_{ISHE} on the microwave frequency and H_{ex} is plotted as a color map in Fig. 3(d). The resonant magnetic field increases monotonically with the frequency, which is consistent with Kittel formula.

DC bias voltage V_{dc} is applied in the sample, as shown in Fig. 3(b). The effect of V_{dc} on the ISHE spectra is plotted in Fig. 4(a). The resonant field $\mu_0 H_{res}$ is monotonically changed from 80 mT to 94 mT by applying V_{dc}. In order to understand the origin of the change of H_{res} on V_{dc}, firstly, the gyromagnetic ratio γ in Eq. (7) is estimated. We used a process similar to a method described by Shaw *et al.* [39], which shows that the error in simultaneous estimation of the effective magnetization M_{eff} and gyromagnetic ratio from the Kittel equation can be minimized by recording the FMR spectra up to H_{ex} well above the M_{eff}. The FMR spectra was detected electrically with an in-plane $\mu_0 H_{ex}$ up to 800 mT along $\phi = 0^o$. H_{res} obtained are plotted as a function of frequency as shown in Fig. 4 (b). In case of $\phi = 0^o$, Eq. (7) reduces to the typical form of Kittel equation as below:

$$f = \gamma\sqrt{(H_{res} + H_k - M_{eff})(H_{res} + H_k)} = \gamma\sqrt{(H_{res} - M_{eff})H_{res}}. \quad (9)$$

The in-plane anisotropy can be assumed to be absent in this process since its effect was found to be negligible for our purposes. We obtain M_{eff} = 50 mT and γ = 0.0298 GHz/mT from the fitting. Furthermore, we could not detect any effect of electric-field on the gyromagnetic ratio in the applied bias voltage range.

Since the gyromagnetic ratio is found to be invariant with V_{dc}, secondly, the change of H_p and H_k on the application of V_{dc} is estimated. The V_{ISHE} spectra were measured as a function of in-plane magnetic field angle ϕ at different bias voltages, as discussed in the previous paragraph. Surprisingly, the sinusoidal amplitude in the ϕ dependence of H_{res}, as shown in Fig. 4(c), is strongly modulated by applying V_{dc}, implying voltage-control for H_k. Upon fitting the experimental data using Eq. (7), it can be observed that H_p and H_k are controlled by bias voltage with a mutually opposite dependence on V_{dc}. Figure 4(d) shows the change of the anisotropy fields and the corresponding anisotropy energies on the left and right axes respectively, as a function of V_{dc} with respect to the unbiased condition (V_{dc} = 0 V) for frequencies from 1.0 GHz to 3.0 GHz. When the top electrode is at a lower potential than the bottom CoFeB electrode (negative bias voltage), H_p is observed to increase, whereas H_k remains almost unchanged. On the other hand, a positive bias voltage decreases H_p and increases H_k.

The penetration depths of the electric-field in metallic ferromagnets is about 0.1 nm and therefore the change of H_p and H_k with bias voltage suggests that PMA and IMA of the

CoFeB/MgO junction are of interfacial origin. VCMA in ferromagnetic metal/oxide interface is understood by a relative change in electron density for the in-plane and out-of-plane oriented 3*d* orbitals of the interfacial ferromagnetic atoms in the presence of an electric-field [40]. The electron filling factor in the d_{z2} orbital is reduced by applying a negative voltage, which leads to increase in PMA. On the other hand, when a positive voltage is applied, the electron filling factors in the out-of plane and in-plane oriented 3*d* orbitals are enhanced and suppressed respectively, leading to a decrease in PMA, accompanied by an increase in IMA. The asymmetric trend of VCMA with respect to the sign of voltage in the samples is predicted for buffer layer/ferromagnetic metal/oxide multilayers which lack spatial inversion symmetry perpendicular to the film plane [41].

V. CONCLUSION

In conclusion, in addition to typical perpendicular magnetic anisotropy of CoFeB/MgO junctions, an interfacial in-plane magnetic anisotropy is observed, whose orientation can be controlled by the direction of applied magnetic field during annealing. Both in-plane and perpendicular magnetic anisotropies could be modulated by electric-fields: a negative bias voltage increases perpendicular magnetic anisotropy, while a positive bias voltage decreases perpendicular magnetic anisotropy and increases the in-plane magnetic anisotropy. This behavior can be understood by a change of electron density for the in-plane and out-of-plane

3*d* orbitals of the ferromagnetic atoms in the presence of electric-field at the CoFeB/MgO junction. So far, the electric-field torque is reported for magnetization direction tilted away from the in-plane and out-of-plane direction of the sample with the application of bias magnetic field. However, our demonstration of voltage controllable in-plane and perpendicular anisotropies of the CoFeB/MgO junction can overcome the requirement of such bias magnetic fields. We believe that such a control of symmetry of the magnetic anisotropy by magnetic annealing and its tunability by electric-fields is a crucial development towards realizing purely voltage-controlled spintronic devices with ultralow power consumption.

ACKNOWLEDGEMENTS

We would like to thank K. Kondou for helpful discussions. This work was supported by Grants-in-Aid (No. 26103002, 16K18079, 18H01862) from JSPS and Materials Science Foundation, Hitachi Metals. B.R. acknowledges RIKEN Incentive Research Project Grant No. FY2019.

References

1. J. S. Slonczewski, *J. Magn. Magn. Mater.* **159**, L1-L7 (1996).
2. L. Berger, *Phys. Rev. B* **54**, 9353-9358 (1996).
3. I. M. Miron, K. Garello, G. Gaudin, P-J. Zermatten, M. V. Costache, S. Auffret, S. Bandiera, B. Rodmacq, A. Schuhl and P. Gambardella, *Nature* **476**, 189-193 (2011).
4. L. Liu, T. Moriyama, D.C. Ralph and R.A. Burhman, *Phys. Rev. Lett.* **106**, 036601 (2011).
5. S. Fukami, T. Anekawa, C. Zhang and H. Ohno, *Nat. Nanotechnol.* **11**, 621-625 (2016).
6. H. Fulara, M. Zahedinejad, R. Khymyn, A.A. Awad, S. Muralidhar, M. Dvornik and J. Akerman, *Science Advances* **5**, 9, eaax8467 (2019).
7. T. Nozaki, Y. Shiota, S. Miwa, S. Murakami, F. Bonell, S. Ishibashi, H. Kubota, K. Yakushiji, T. Saruya, A. Fukushima, S. Yuasa, T. Shinjo and Y. Suzuki, *Nat. Phys.* **8**, 491–496 (2012).
8. F. Matsukura, Y. Tokura and H. Ohno, *Nat. Nanotechnol.* **10,** 209-220 (2015).
9. S. S. P. Parkin, C. Kaiser, A. Panchula, P.M. Rice, B. Hughes, M. Samant and S-H. Yang, *Nat. Mater.* **3**, 862-867 (2004).
10. S. Yuasa, T. Nagahama, A. Fukushima, Y. Suzuki and K. Ando, *Nat. Mater.* **3**, 868-871 (2004).
11. S. Ikeda, K. Miura, H. Yamamoto, K. Mizunuma, H.D. Gan, M. Endo, S. Kanai, J. Hayakawa, F. Matsukura and H. Ohno, *Nat. Mater.* **9**, 721–724 (2010).
12. Y. Shiota, T. Nozaki, F. Bonell, S. Murakami, T. Shinjo and Y. Suzuki, *Nat. Mater.* **11**, 39–43 (2012).
13. J. Zhu, J.A. Katine, G. E. Rowlands, Y-J. Chen, Z. Duan, J.G. Alzate, P. Upadhyaya, J. Langer, P.K. Amiri, K.L. Wang and I.N. Krivorotov, *Phys. Rev. Lett.* **108**, 197203 (2012).
14. C. Grezes, F. Ebrahimi, J.G. Alzate, X. Cai, J.A. Katine, J. Langer, B. Ocker, P.K. Amiri and K.L. Wang, *Appl. Phys. Lett.* **108**, 012403 (2016).

15. S. Kanai, F. Matsukura and H. Ohno, *Appl. Phys. Lett.* **108**, 192406 (2016).
16. K. Miura, S. Yabuuchi, M. Yamada, M. Ichimura, B. Rana, S. Ogawa, H. Takahashi, Y. Fukuma and Y. Otani, *Sci. Rep.* **7**, 42511 (2017).
17. B. Rana, Y. Fukuma, K. Miura, H. Takahashi and Y. Otani, *Appl. Phys. Lett.* **111**, 052404 (2017).
18. P. Bruno, *Phys. Rev. B* **39**, 865 (1989).
19. H.X. Yang, M. Chshiev, B. Dieny, J.H. Lee, A. Manchon and K.H. Shin, *Phys. Rev. B* **84**, 054401 (2011).
20. D. Chiba, M. Sawicki, Y. Nishitani, Y. Nakatani, F. Matsukura and H. Ohno, *Nature* **455**, 515-518 (2008).
21. K.Ohta, T. Maruyama, T. Nozaki, M. Shiraishi, T. Shinjo, Y. Suzuki, S.-S. Ha, C.-Y. You and W. Van Roy, *Appl. Phys. Lett.***94**, 032501 (2009).
22. J. Smit and H.G. Beljers, *Philips Res. Repts.* **10**, 113-130 (1955).
23. W. X. Wang, Y. Yang and H. Naganuma, Y. Ando, R.C. Yu, X.F. Han, *Appl. Phys. Lett.* **99**, 012502 (2011).
24. D. C. Worledge, G. Hu, D.W. Abraham and P.L. Trouilloud, S. Brown, *J. Appl. Phys.* **115**, 172601 (2014).
25. S. Chikazumi, International series of monographs on physics 94: Physics of Ferromagnetism. *Oxford University Press* (2009).
26. L. Neel, *J. de phys.*, **15,** 225-239 (1954).
27. S. Taniguchi, *Sci. Rep. Res. Inst. Tohoku Uinv.* **A7,** 269-281 (1955).
28. S. Chikazumi and T. Oomura, *J. Phys. Soc. Japan.* **10**, -849 (1955).
29. S. V. Karthik, Y. K. Takahashi, T. Ohkubo, K. Hono, S. Ikeda and H. Ohno, *J. Appl. Phys.* **106**, 023920 (2009).

30. I. Barsukov, Y. Fu, C. Safranski, Y.-J. Chen, B. Youngblood, A.M. Goncalves, M. Spasova, M. Farle, J.A. Katine, C.C. Kuo and I.N. Krivorotov, *Appl. Phys. Lett.* **106**, 192407 (2015).
31. F.M. Dyson, Phys. Rev. **102**, 5 (1956).
32. J. G. Alzate, P.K. Amiri, G. Yu, P. Upadhyaya, J.A. Katine, J. Langer, B. Ocker, I.L. Krivorotov and K.L. Wang, *Appl. Phys. Lett.* **104**, 112410 (2014).
33. H.B. Callen and E. Callen, *J. Phys. Chem. Solids* **27**, 1271 (1966).
34. Y. Fu, I. Barkukov, J. Li, A.M. Goncalves, C.C. Kuo, M. Farle and I.N. Krivorotov, *Appl. Phys. Lett.* **108**, 142403 (2016).
35. H. Sato, P. Chureemart, F. Matsukura, R.W. Chantrell, H. Ohno and R.F.L. Evans, *Phys. Rev. B* 98, 214428 (2018).
36. Z. Wen, H. Sukegawa, T. Seki, T. Kubota, K. Takanashi and S. Mitani, *Sci. Rep.* **7**, 45026 (2017).
37. M. Harder, Y. Gui, and C.-M. Hu, *Phys. Rep.* **661**, 1-59 (2016).
38. S. Gupta, R. Medwal, D. Kodama, K. Kondou, Y. Otani and Y. Fukuma, *Appl. Phys. Lett.* **110**, 022404 (2017).
39. J.M. Shaw, H.T. Nembach, T.J. Silva and C.T. Boone, *J. Appl. Phys.* **114**, 243906 (2013).
40. T. Maruyama, Y. Shiota, T. Nozaki, K. Ohta, N. Toda, M. Mizuguchi, A.A. Tulapurkar, T. Shinjo, M. Shiraishi, Y. Ando and Y. Suzuki, *Nat. Nanotechnol.* **4**, 158-161 (2009).
41. R. Shimabukuro, K. Nakamura, T. Akiyama and T. Ito, *Phys. E* **42,** 1014-1017 (2010).

Figure legends

FIG. 1. (a) Schematic of the experimental setup used to detect FMR signal depicting the axes, ground (G) and signal (S) terminals of the co-planar waveguide (CPW) and the direction of the applied microwave field h_{rf}. Below a typical FMR spectra is shown that consists of imaginary and real parts of reflection parameter S_{11} (symbols) with fits to Eq. (8) (line). **(b)** In-plane angle ϕ dependence of the resonant field H_{res} (squares) at frequency f = 8.0 GHz for a 2.0-nm thick CoFeB layer annealed at 200 °C in presence of a magnetic field H_b in three orthogonal directions (arrows of corresponding color on the block in inset). Lines are fits to Eq. (7). **(c)** In-plane magnetic anisotropy field H_k plotted (solid symbols) as a function of annealing temperature for CoFeB layers with thicknesses ranging from 1.5 nm to 2.0 nm. **(d)** Corresponding perpendicular magnetic anisotropy H_p for the samples. Error bars represent the maximum deviation of the anisotropy fields obtained for different frequencies from the average value.

FIG. 2. (a) Saturation magnetization M_s as a function of temperature. Upon fitting using Bloch's law, T_C = 1150 K and χ = 1.5 is obtained for T < 50 K (green line) and T_C = 1150 K and χ = 1.8 for T > 50 K (red line). **(b)** Temperature dependence of anisotropy fields H_p (red squares) and H_k (black squares). **(c)** Anisotropy energies $K_{u\perp}$ (red squares) and $K_{u//}$ (black squares) corresponding to H_p and H_k are plotted as a function of temperature. Lines are fits to power law of magnetization given by the Callen-Callen relation (lines) with γ = 2.1 and 2.3

for $K_{u\perp}$ and $K_{u//}$. Error bars represent maximum deviation of the anisotropy fields and corresponding energies obtained for different frequencies from the average value.

FIG. 3. (a) Optical microscope image of the device used for electrical detection of FMR under bias voltages. **(b)** Schematic of the experimental setup used to detect FMR signal electrically via spin pumping and inverse spin Hall effect (ISHE). Spin current generated from the CoFeB layer by spin pumping is converted into a charge current due to ISHE of Ta and then gives rise to a rectified voltage V_{ISHE}. The Ti/Au top electrode allows us to apply a bias voltage V_{dc} at the CoFeB/MgO interface. **(c)** External magnetic field H_{ex} dependence of V_{ISHE} at different frequencies. **(d)** Color-coded V_{ISHE} spectra.

FIG. 4. (a) Dependence of V_{ISHE} spectra on bias voltage V_{dc} at $f = 2.0$ GHz (symbols). The lines are fits to experimental data by using Eq. (8). **(b)** Resonance fields H_{res} as a function of f (symbols) with fits to Eq. (9). **(c)** In plane angle ϕ dependence of H_{res} at different V_{dc} at $f = 2.0$ GHz. The lines are fits to experimental data using Eq. (7). **(d)** The change of anisotropy fields $\mu_o \Delta H_{ani}$ (symbols with lines) with respect to V_{dc} is shown on the left while the corresponding change in energies ΔK_u is shown on the right axis. PMA and IMA refer to perpendicular and in-plane magnetic anisotropy respectively.

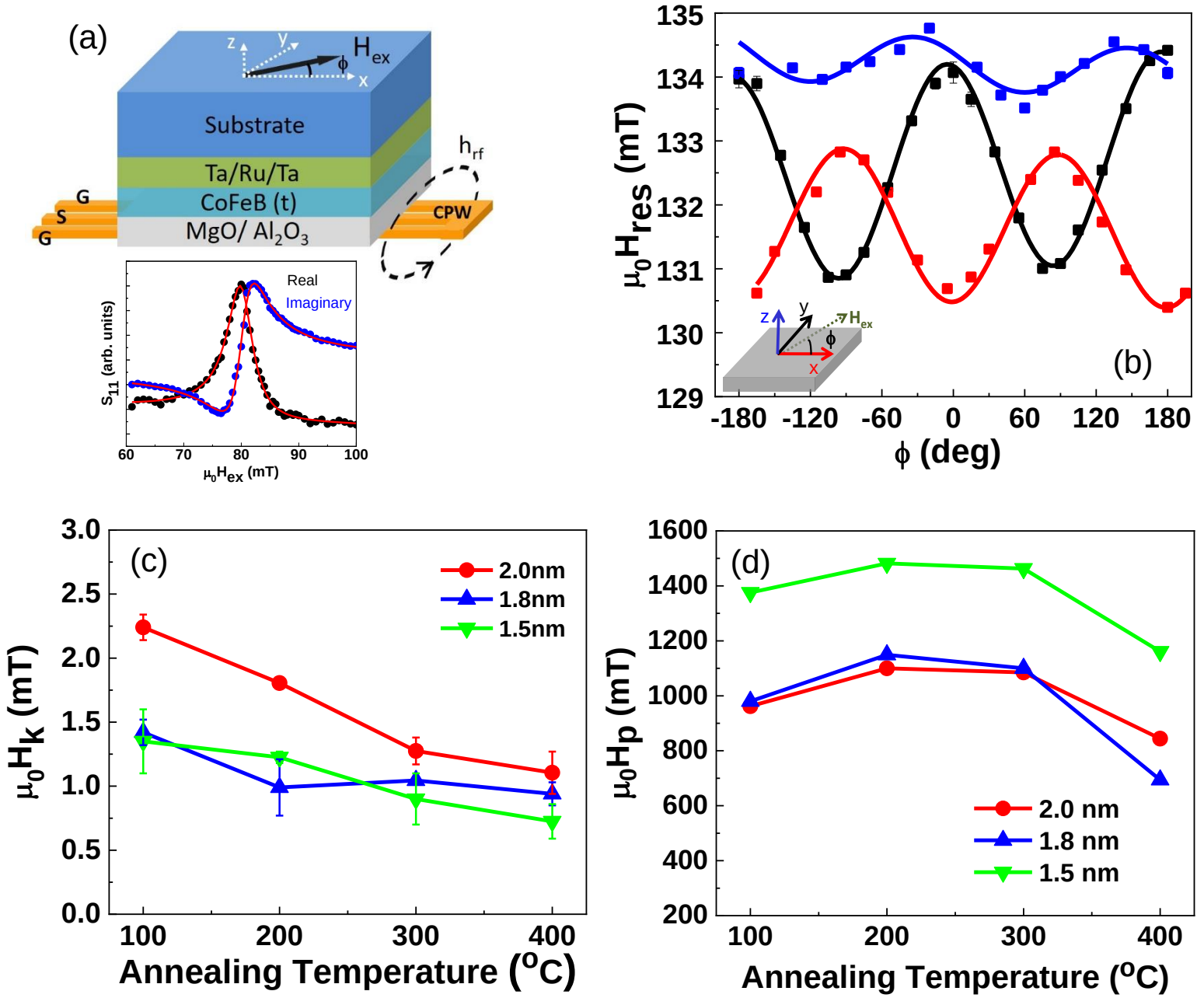

Fig. 1, A. Deka *et al.*

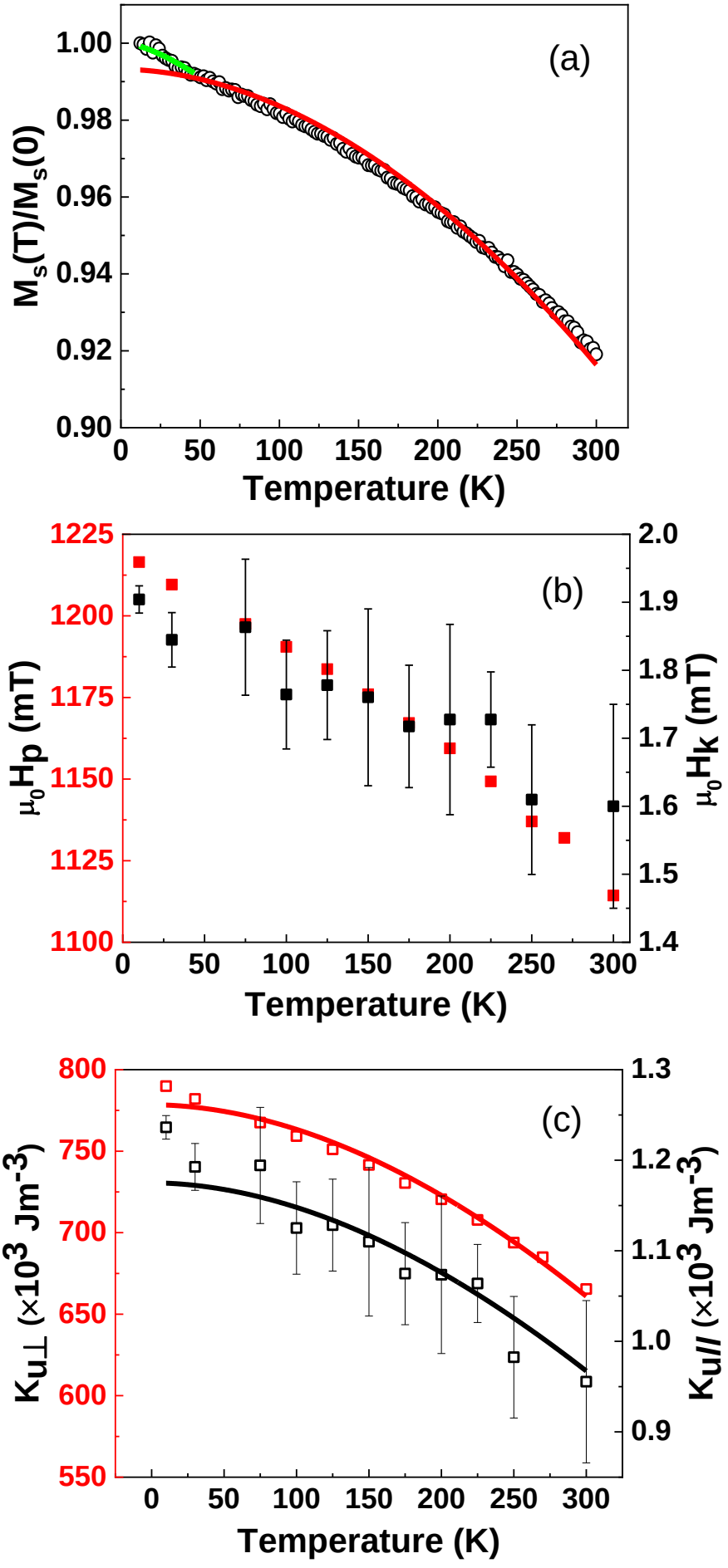

Fig. 2, A. Deka *et al.*

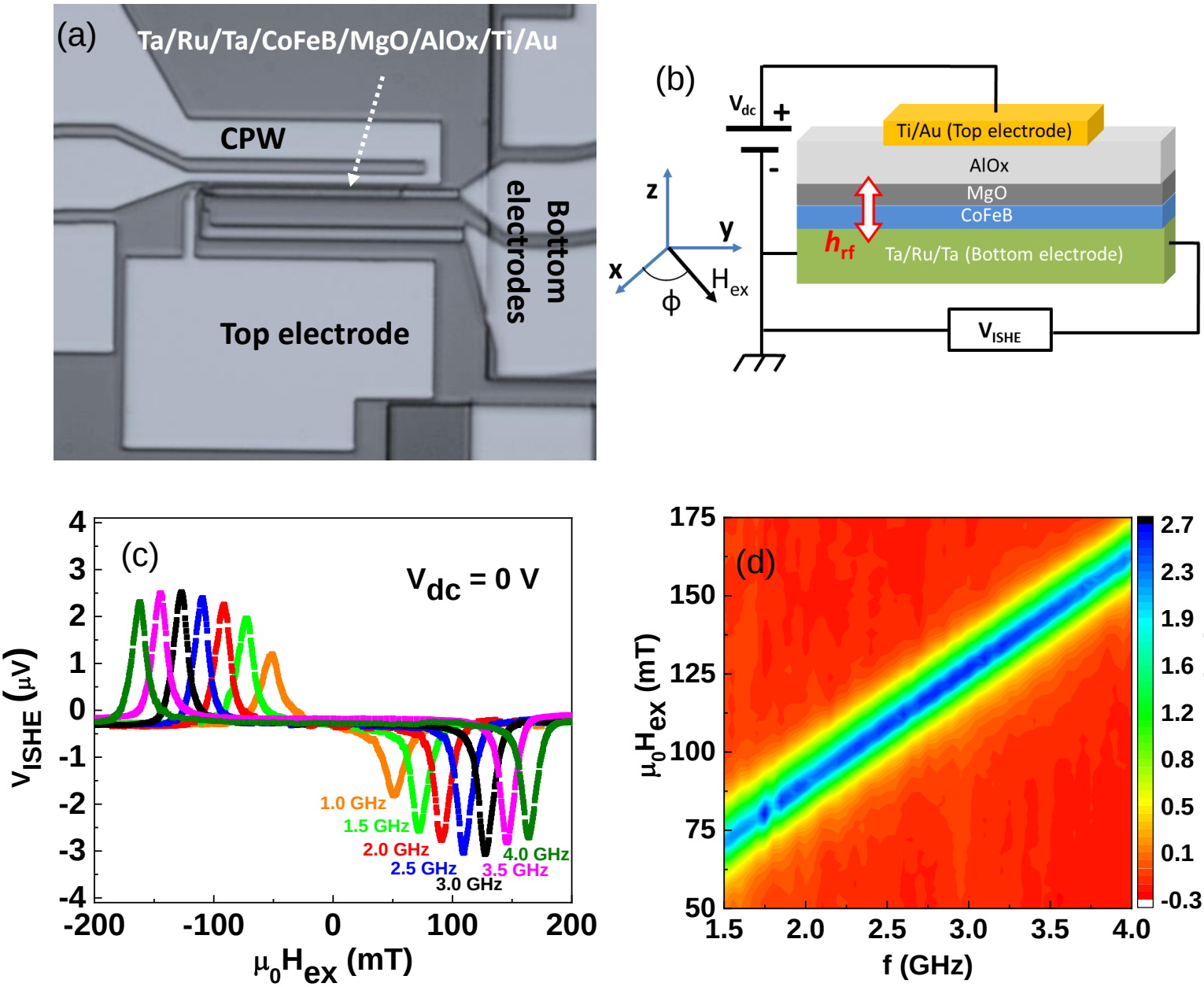

Fig. 3, A. Deka *et al.*

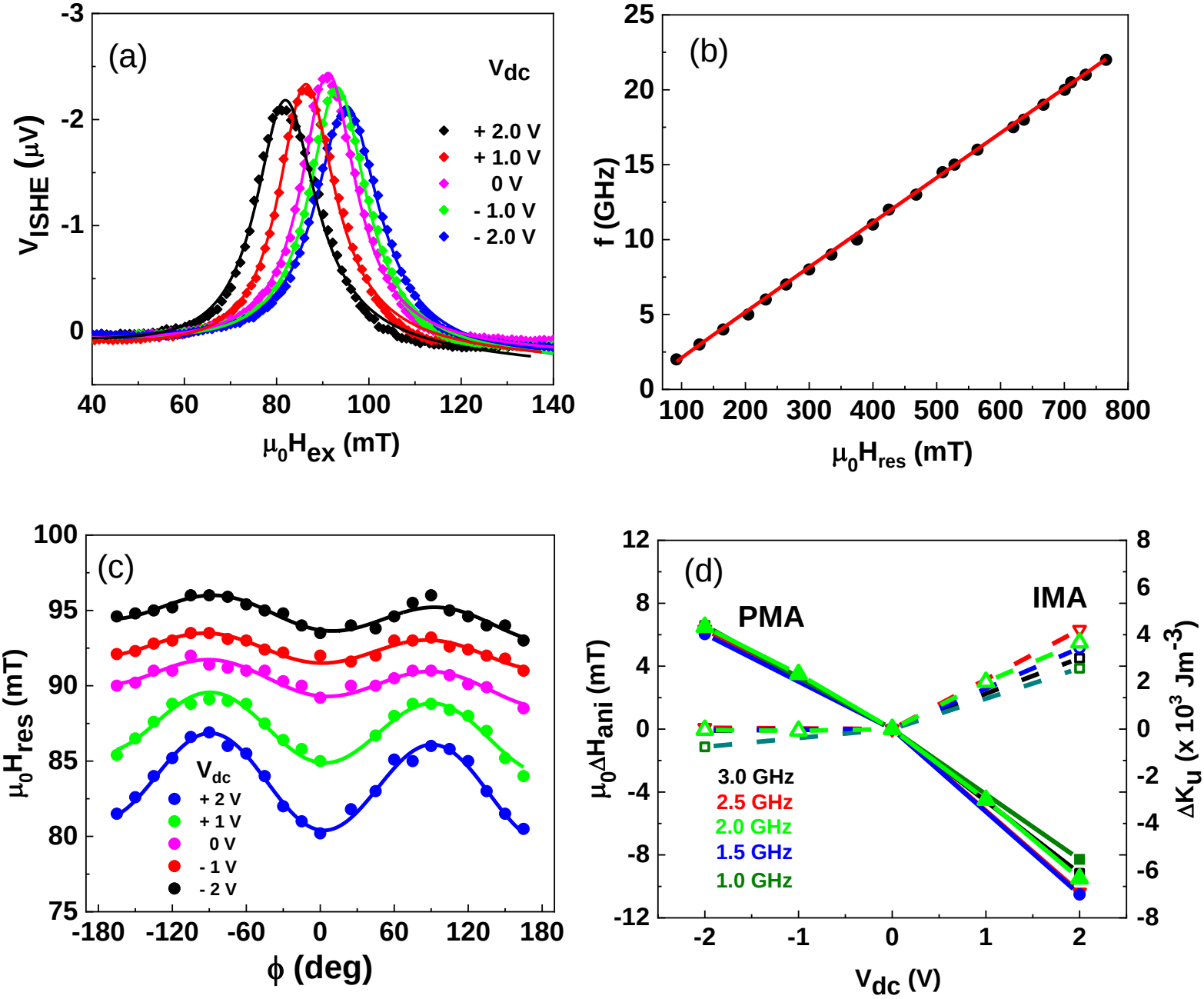

Fig. 4, A. Deka *et al.*